

# Nucleon-nucleon momentum correlation function as a probe of the density distribution of valence neutron in neutron-rich nucleus

X. G. Cao,<sup>1</sup> X. Z. Cai\*,<sup>1</sup> Y. G. Ma†,<sup>1</sup> D. Q. Fang,<sup>1</sup> G. Q. Zhang,<sup>1,2</sup> W. Guo,<sup>1</sup> J. G. Chen,<sup>1</sup> and J. S. Wang<sup>3</sup>

<sup>1</sup>Shanghai Institute of Applied Physics, Chinese Academy of Sciences, Shanghai 201800, China

<sup>2</sup>Graduate School of the Chinese Academy of Sciences, Beijing 100049, China

<sup>3</sup>Institute of Modern Physics, Chinese Academy of Sciences, Lanzhou 730000, China

(Dated: November 30, 2012)

Proton-neutron, neutron-neutron and proton-proton momentum correlation functions ( $C_{pn}$ ,  $C_{nn}$ ,  $C_{pp}$ ) are systematically investigated for  $^{15}\text{C}$  and other C isotopes induced collisions at different entrance channel conditions within the framework of the isospin-dependent quantum molecular dynamics (IDQMD) model complemented by the CRAB (correlation after burner) computation code.  $^{15}\text{C}$  is a prime exotic nucleus candidate due to the weakly bound valence neutron coupling with closed-neutron shell nucleus  $^{14}\text{C}$ . In order to study density dependence of correlation function by removing the isospin effect, the initialized  $^{15}\text{C}$  projectiles are sampled from two kinds of density distribution from RMF model, in which the valence neutron of  $^{15}\text{C}$  is populated on both  $1d5/2$  and  $2s1/2$  states, respectively. The results show that the density distributions of valence neutron significantly influence nucleon-nucleon momentum correlation function at large impact parameter and high incident energy. The extended density distribution of valence neutron largely weakens the strength of correlation function. The size of emission source is extracted by fitting correlation function using Gaussian source method. The emission source size as well as the size of final state phase space is larger for projectiles sampling from more extended density distribution of valence neutron corresponding  $2s1/2$  state in RMF model. Therefore momentum correlation function can be considered as a potential valuable tool to diagnose the exotic nuclear structure such as skin and halo.

PACS numbers: 25.60.-t, 25.70.Pq, 21.10.Gv

## I. INTRODUCTION

Intensity interferometry method, developed by Hanbury Brown and Twiss (HBT) in 1950s [1], was originally used to measure astronomical objects such as angular diameter of stars. The method was later introduced into subatomic physics by Goldhaber *et al.*, who extracted the spatial extent of an annihilation fireball in proton-antiproton reactions by two-pion correlations [2]. Then the method was widely applied in exploring the nuclear reactions from low-energy to relativistic-energy [3–10]. Recently, it has been extended to other fields, for instance, the analogous correlations describing the fermionic statics of elections [11, 12].

In heavy ion collisions (HICs) at intermediate energy, the HBT method is widely used to extract the space-time properties such as the source size and emission time of fragments by two-particle correlation functions [13, 14]. The dependences of momentum correlation function on the impact parameter [15, 16], the total momentum of nucleon pairs [16, 17], the isospin of the emitting source [18], the nuclear symmetry energy [19] and the nuclear equation of state (EOS) [16] are also explored by experiment and theory.

Besides the applications of two-particle momentum

correlation functions to investigate heavy ion collision process, the HBT method is also extended to study exotic structure of nuclei far from the  $\beta$ -stability line due to the rapid development of radioactive nuclear beams. The neutron-neutron correlation functions ( $C_{nn}$ ) of Borromean halo nuclei such as  $^6\text{He}$ ,  $^{11}\text{Li}$  and  $^{14}\text{Be}$  are constructed to extract the size of separation between the two halo neutrons [20–25]. In addition, Wei and Ma *et al.* found that the strength of proton-neutron momentum correlation functions at small relative momentum has linear dependence on binding energy per nucleon or single neutron separation energy for light isotope chains [16, 26, 27]. The analogous suppressed proton-proton correlation function is also suggested as another potential tool to diagnose proton halo nuclei [28] beside the conventional methods such as total reaction cross section and momentum distribution width measurements [29, 30]. Ma *et al.* have carried our experiment on RIPS in RIKEN to measure the proton-proton momentum correlation function for revealing the exotic structure of proton-rich nucleus  $^{23}\text{Al}$  [31, 32]. Therefore, it is very interesting to investigate how the exotic structure affects the nucleon-nucleon momentum correlation function, which can serve as a potential observable to extract information about anomalous structure in nucleus.

In this paper, we calculated  $^{15}\text{C} + ^{12}\text{C}$  collisions by IDQMD model.  $^{15}\text{C}$  is a one-neutron halo candidate because of its small neutron separation energy:  $S_n = 1.218$  MeV [33], closed-neutron shell core:  $^{14}\text{C}$ , narrower momentum distribution of  $^{14}\text{C}$  fragment from the breakup of

\*E-mail address: caixz@sinap.ac.cn

†E-mail address: ygma@sinap.ac.cn

$^{15}\text{C}$  [34, 35] and larger  $s$ -wave spectroscopic factor of  $^{15}\text{C}$  ground state [36] by  $^{14}\text{C}(d,p)^{15}\text{C}$  reaction measurement. However, a consistent picture have not been obtained in reaction cross section measurement. The interaction cross section ( $\sigma_I$ ) do not have peculiarity compared with neighbor isotopes at incident energy 740 MeV/nucleon [37]. However, reaction cross section ( $\sigma_R$ ) shows more or less enhancement at intermediate energies and there is also a large difference factor ( $d$ ) for  $\sigma_R$  [35, 38], which is defined as [39]:  $d = \frac{\sigma_R(\text{exp}) - \sigma_R(G)}{\sigma_R(G)}$ , where  $\sigma_R(\text{exp})$  represents intermediate energy experimental  $\sigma_R$  and  $\sigma_R(G)$  is the  $\sigma_R$  calculated by the Glauber Model at the same bombarding energy with HO-type density distribution, which is obtained by fitting experimental  $\sigma_R$  at high energy. The  $s$ -wave spectroscopic factor extracted from  $\sigma_I$  is also different from the value obtained from transfer reaction. Fang *et al.* found that  $s$ -wave component is dominant in the ground state of  $^{15}\text{C}$  by simultaneous measurement of  $\sigma_R$  and momentum distribution [35]. However, the fitted results by the Glauber model are deviated from the experimental data at low energies for  $\sigma_R$ . Therefore, new probes are needed to estimate the density distribution of valence neutron in  $^{15}\text{C}$  and other analogous neutron-rich exotic nucleus candidates.

The initialized  $^{15}\text{C}$  projectiles are sampled from densities calculated by RMF model to study how density distributions of outer neutron affect nucleon-nucleon momentum correlation function. In RMF model, the last neutron of  $^{15}\text{C}$  is populated on both  $1d5/2$  and  $2s1/2$  states, respectively. Because the isospin degree of freedom is removed, the relationship between the momentum correlation function and the structure of exotic nuclei such as skin can be more directly explored by comparing different collisions induced by different configured  $^{15}\text{C}$  projectiles.

The rest part of this paper is organized as follows: in Sec. II, we briefly describe the HBT technique and the IDQMD model; the initialization of  $^{15}\text{C}$  projectiles and nucleon-nucleon momentum correlation function of different configured C isotopes induced collisions are discussed in Sec. III; the summary is presented in Sec. IV.

## II. HBT TECHNIQUE AND IDQMD MODEL

### A. HBT technique

It is known that the final-state interaction (FSI) and quantum-statistical symmetry (QSS) affect the wave function of relative motion of light identical particles when they are emitted in close region in phase-space and time, which is the principle of intensity interferometry, i.e., the HBT method. The correlation function of two-particle can be obtained by convolution of emission func-

tion  $g(\mathbf{p}, x)$  in standard *Koonin-Pratt* equation [3–5]:

$$C(\mathbf{P}, \mathbf{q}) = \frac{\int d^4x_1 d^4x_2 g(\mathbf{P}/2, x_1) g(\mathbf{P}/2, x_2) |\phi(\mathbf{q}, \mathbf{r})|^2}{\int d^4x_1 g(\mathbf{P}/2, x_1) \int d^4x_2 g(\mathbf{P}/2, x_2)}, \quad (1)$$

where  $\mathbf{P} (= \mathbf{p}_1 + \mathbf{p}_2)$  and  $\mathbf{q} (= (\mathbf{p}_1 - \mathbf{p}_2)/2)$  are the total and relative momentum of particle pair, respectively,  $g(\mathbf{p}, x)$  is the probability of emitting a particle with momentum  $\mathbf{p}$  at space-time point  $x(\mathbf{r}, t)$  and  $\phi(\mathbf{q}, \mathbf{r})$  is two-particle relative wave function with relative distance  $\mathbf{r} = (\mathbf{r}_2 - \mathbf{r}_1) - \frac{1}{2}(\mathbf{v}_1 + \mathbf{v}_2)(t_2 - t_1)$ .

In specific application of the Koonin-Pratt formula, the reliable single-particle phase space distribution at freeze-out stage is needed [15]. In this paper, the IDQMD model is used as event generator. It is a widely used transport model in intermediate energy HICs and has also been successfully applied to HBT studies for neutron-rich nuclei induced reactions by Wei and Ma *et al.* [16, 26–28]. The phase space of emitted particles is used as the input of Pratt's CRAB (correlation after burner) code [40], which takes the FSI and QSS effects into account for remedying the disadvantage of semi-classical transport model.

### B. IDQMD model

The quantum molecular dynamics (QMD) approach is a many-body theory that can describe HICs from intermediate to relativistic energies [41–43]. The main advantage of the QMD model is that it can explicitly treat many-body state of the collision system, so it contains correlation effects to all orders. Therefore, the QMD model provides valuable information about both the collision dynamics and the fragmentation process. The model also has excellent extensibility due to its microscopic treatment of collision process. It mainly consists of several parts: initialization of the projectile and the target nucleons, propagation of nucleons in the effective potential, nucleon-nucleon (NN) collisions in a nuclear medium, the Pauli blocking and the numerical test.

The IDQMD model is based on QMD model and affiliates the isospin factors in mean field, two-body NN collisions and Pauli blocking [16, 26, 44–47]. In addition, the phase space sampling of neutrons and protons in the initialization should be separately treated because of the large difference between neutron and proton density distributions for nuclei far from the  $\beta$ -stability line. In order to properly incorporate nuclear structure effects into microscopic simulations, stable initialized  $^{15}\text{C}$  with and without neutron-halo structure have been sampled.

In IDQMD model, each nucleon is represented by a Gaussian wave packet with width  $\sqrt{L}$  (here  $L = 2.16 \text{ fm}^2$ ) centered around the mean position  $\vec{r}_i(t)$  and the mean momentum  $\vec{p}_i(t)$ :

$$\psi_i(\vec{r}, t) = \frac{1}{(2\pi L)^{3/4}} \exp\left[-\frac{(\vec{r} - \vec{r}_i(t))^2}{4L}\right] \exp\left[\frac{i\vec{r} \cdot \vec{p}_i(t)}{\hbar}\right]. \quad (2)$$

Then all nucleons interact via mean field and NN collisions. The nuclear mean field is parameterized by

$$U(\rho, \tau_z) = \alpha \left( \frac{\rho}{\rho_0} \right) + \beta \left( \frac{\rho}{\rho_0} \right)^\gamma + \frac{1}{2} (1 - \tau_z) V_c + C_{sym} \frac{\rho_n - \rho_p}{\rho_0} \tau_z + U^{Yuk}, \quad (3)$$

with  $\rho_0 = 0.16 \text{ fm}^{-3}$  (the normal nuclear matter density).  $\rho$ ,  $\rho_n$  and  $\rho_p$  are the total, neutron and proton densities, respectively.  $\tau_z$  is  $z$ th component of the isospin degree of freedom, which equals 1 or -1 for neutrons or protons, respectively. The coefficients  $\alpha$ ,  $\beta$  and  $\gamma$  are parameters of nuclear equation of state (EOS).  $C_{sym}$  is the symmetry energy strength due to the difference between neutron and proton, taking the value of 32 MeV. In this work,  $\alpha = -356 \text{ MeV}$ ,  $\beta = 303 \text{ MeV}$  and  $\gamma = 7/6$  are taken, which corresponds to the so-called soft EOS with [42].  $V_c$  is the Coulomb potential and  $U^{Yuk}$  is Yukawa (surface) potential, which has the following form:

$$U^{Yuk} = \frac{V_y}{2m} \sum_{i \neq j} \frac{1}{r_{ij}} \exp(Lm^2) \times [\exp(-mr_{ij}) \text{erfc}(\sqrt{L}m - r_{ij}/\sqrt{4L}) - \exp(mr_{ij}) \text{erfc}(\sqrt{L}m + r_{ij}/\sqrt{4L})], \quad (4)$$

with  $V_y = -0.0074 \text{ GeV}$ ,  $m = 1.25 \text{ fm}^{-1}$  and  $r_{ij} = |\vec{r}_i - \vec{r}_j|$  is the relative distance between two nucleons. Experimental parameterized NN cross section, which is energy and isospin dependent, is used.

The Pauli blocking effect in IDQMD model is also isospin dependent. The blocking of neutron and proton is separately treated as follows: each nucleon occupies a six-dimensional sphere with a volume of  $\hbar^3/2$  in the phase space (considering the spin degree of freedom) and we calculate the phase space volume ( $V$ ) of the scattered nucleons being occupied by the rest nucleons with the same isospin as that of the scattered ones. We then compare  $2V/\hbar^3$  with a random number and decide whether the collision is blocked or not.

The time evolution of the colliding system is given by the generalized variational principle. Nuclear clusters are constructed by a coalescence model, in which particles with relative momentum smaller than  $P_0$  and relative distance smaller than  $R_0$  are considered to belong to one cluster. The parameter set:  $P_0 = 300 \text{ MeV}/c$  and  $R_0 = 3.5 \text{ fm}$  is taken here.

### III. THE INITIALIZATION OF $^{15}\text{C}$ PROJECTILES AND SYSTEMATICAL HBT RESULTS

In IDQMD, the initialization of projectiles and targets distinct proton from neutron. We sample the nucleon's coordinates from density distributions of proton

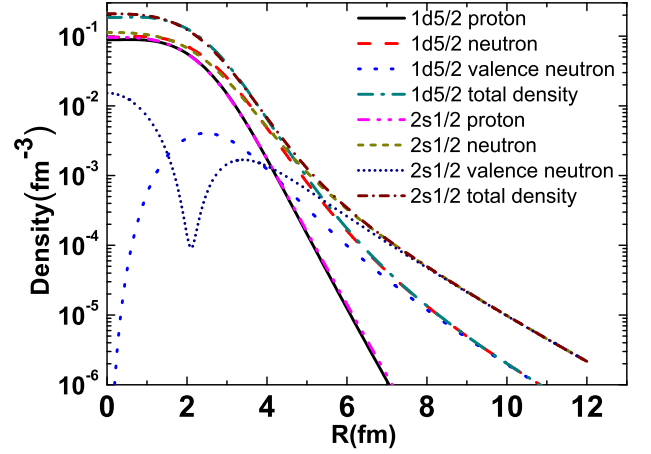


FIG. 1: (Color online) The proton, neutron, valence neutron and total density distributions of  $^{15}\text{C}$  for the valence neutron on  $1d5/2$  and  $2s1/2$  states, respectively, by RMF calculations.

TABLE I: RMS radii of initialized  $^{15}\text{C}$  by RMF theory and experimental RMS charge radius of  $^{14}\text{C}$ . The RMS radii of  $^{15}\text{C}$  projectiles are initialized to match with the values in this table.

	Z	N	Valence N	$^{14}\text{C}$ core	$^{15}\text{C}$	$^{14}\text{C}$ exp. [48]
	(fm)	(fm)	(fm)	(fm)	(fm)	(fm)
$^{15}\text{C}$						2.50
( $1d5/2$ )	2.40	2.76	3.85	2.51	2.62	
$^{15}\text{C}$						
( $2s1/2$ )	2.39	2.96	5.01	2.51	2.75	

and neutron, which are calculated by relativistic mean field (RMF) method. Fig. 1 shows the proton, neutron, valence neutron and total density distributions of two different configured  $^{15}\text{C}$  projectiles, whose valence neutron is assigned on both  $1d5/2$  and  $2s1/2$  states, respectively. It can be seen that the valence neutron on  $2s1/2$  state has longer tail than that on  $1d5/2$  state while proton almost has the same density distributions for two case. The effect of more extended valence neutron density distribution can be reflected by nucleon-nucleon momentum correlation function as showed below.

In our calculations, initialization of  $^{15}\text{C}$  is carefully controlled. The stability of the sampled  $^{15}\text{C}$  projectiles is strictly checked by time evolution in mean field till  $200 \text{ fm}/c$  at zero temperature according to the average binding energies, root-mean-square (RMS) radii and density distributions of neutron and proton. Eligible initialization samples should meet the following requirements till  $200 \text{ fm}/c$ : a) average binding energy needs to match with experimental data; b) RMS radius also needs to be in according with RMF result; c) the difference of neutron tails between two kinds of  $^{15}\text{C}$  projectiles should keep all the way. To better imitate input density from RMF calculation and reflect the structure effect, thousands of eligible initialized samples are accumulated to simulating collisions. The initialized samples of other C

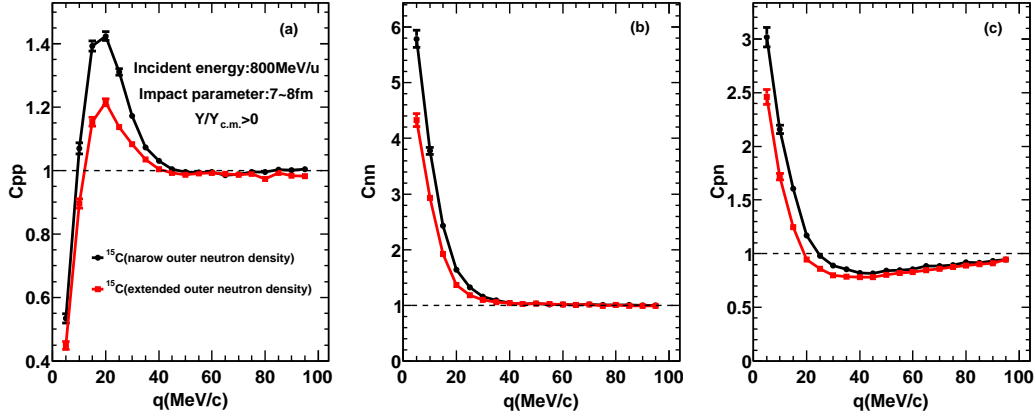


FIG. 2: (Color online) Proton-proton ( $C_{pp}$ , panel (a)), neutron-neutron ( $C_{nn}$ , panel (b)) and proton-neutron ( $C_{pn}$ , panel (c)) momentum correlation functions as a function of relative momentum, which are calculated at incident energy of 800 MeV/nucleon, impact parameter  $b = 7 - 8 fm$  and selected nucleons with rapidity  $> 0$ . The circles and squares represent two different kinds of initialized  $^{15}C$  projectiles induced collisions, where  $^{15}C$  projectiles are sampled from two density outputs of RMF model with valence neutron on  $1d5/2$  and  $2s1/2$  states, respectively. The dashed line is used to guide the eyes.

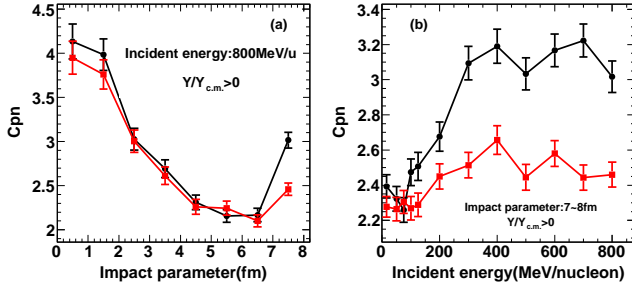


FIG. 3: (Color online) (a):  $C_{pn}$  strength at 5 MeV/c as a function of impact parameter, which is calculated at incident energy of 800 MeV/nucleon and selected nucleons with rapidity  $> 0$ ; (b):  $C_{pn}$  strength at 5 MeV/c as a function of incident energy, which is calculated at impact parameter  $b = 7 - 8 fm$  and selected nucleons with rapidity  $> 0$ . The symbols in both panel (a) and (b) have the same convention as in Fig. 2.

isotopes are prepared in a similar way above.

Even with very elaborate initialization, the tail of density in QMD model can not be reproduced very well compared with RMF model since the wave function in QMD model has Gaussian form. However, the obvious differences of neutron tails between two kinds of  $^{15}C$  projectiles can keep stable enough and thus it can play the role of skin structure in collisions. In the following, we will present how the skin structure expressed by different neutron density distributions in QMD affects nucleon-nucleon momentum correlations.

The proton and neutron phase space of  $^{15}C + ^{12}C$  collisions at freeze-out time generated by IDQMD model, is used as input to CRAB code. The obtained proton-proton, neutron-neutron and proton-neutron momentum correlation functions are shown in Fig. 2, respectively, where  $q$  denotes relative momentum of nucleon pair. As expected,  $C_{nn}$  and  $C_{pn}$  peak at small  $q$  while proton-proton is anti-correlation at small  $q$  owing to the

Coulomb potential and antisymmetrization. The peak of  $C_{pp}$  at 20 MeV/c is due to  $s$ -partial wave of the proton-proton scattering, which strongly depends on the size of emitting source. Our simulations pretty well reproduce the shape and height of  $C_{pp}$ ,  $C_{nn}$  and  $C_{pn}$  vs.  $q$  compared with experimental cases [14]. It can be seen that  $C_{nn}$  and  $C_{pn}$  are both largely reduced at small  $q$  because of the more extended neutron density distribution. In Fig. 2, the size of emission source is mostly decided by projectile-like remnants since we adopt impact parameter  $b = 7 - 8 fm$  and rapidity  $> 0$ . The RMS radii of proton, neutron, valence neutron,  $^{14}C$  core,  $^{15}C$  by RMF calculation and experimental RMS charge radius of  $^{14}C$  are shown in table I. The RMS radii of initialized  $^{15}C$  projectiles are required to meet the RMF calculated values. Though there is no available experimental RMS radius of  $^{15}C$ , RMS radius of  $^{14}C$  core reproduces experimental RMS charge radius of  $^{14}C$  quite well. The RMS radii of  $^{15}C$  do not have large difference for two kinds of  $^{15}C$  projectiles. However, the corresponding RMS radii of valence neutron are  $3.85 fm$  and  $5.01 fm$ . Therefore, the strength of momentum correlation functions can indeed sensitively reflect the fine difference of neutron density distribution. Although the density distributions of proton for two configured  $^{15}C$  are almost the same (as seen in Fig. 1),  $C_{pp}$  still has large differences, which demonstrate that the proton density distribution has changed when proton emission. The density distributions of neutrons and protons are coupling with each other during collisions.

The impact parameter dependence of  $C_{pn}$  at 800 MeV/nucleon incident energy for the two different kinds of initialized  $^{15}C$  projectiles is shown in panel (a) of Fig. 3. The strength of correlation becomes decreasing with  $b$  up to  $6.5 fm$ . In central collisions, emitted nucleons have stronger correlations between themselves because they come from one compact, hot and dense region, which is consistent with previous Boltzmann-Uehling-Uhlenbeck

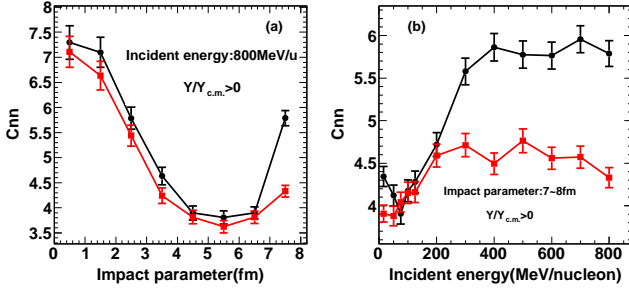


FIG. 4: (Color online) The same as Fig. 3 but for  $C_{nn}$ .

(BUU) [15, 49] and IDQMD [16] results. In peripheral collisions with  $b > 6.5 fm$  the rapid enhancement of  $C_{pn}$  reveals different collisions dynamics from central collisions. This is due to the fact that there is no bulk overlap region at large impact parameter and only the outer nucleons of  $^{15}C$  are scraped. They keep more initial structure information of projectile. Thus, there exists strong correlation among these nucleons. The difference of  $^{15}C$  in neutron density distribution such as skin structure can be well revealed in peripheral collisions while the small difference of density is wiped away in violent central and semi-peripheral collisions.

How incident energy affects  $C_{pn}$  is represented in panel (b) of Fig. 3. The correlations for both cases increase from very low incident energy and then almost reach saturation above 300 MeV/nucleon. This is understandable due to the fact that increasing incident energies lead to more rapid collision process and there is smaller space and time interval among emitting nucleons [16, 49], which leads to stronger correlation. The apparent differences in  $C_{pn}$  exist for the two kinds of  $^{15}C$  induced collisions above saturation energy. The saturation of  $C_{pn}$  at high incident energies and the large differences provide us the proper entrance channel conditions to explore the relation between initial structure and final effect.

The impact parameter and incident energy dependences of  $C_{nn}$  are shown in panel (a) and panel (b) of Fig. 4, respectively. The tendency of  $C_{nn}$  is similar to  $C_{pn}$  for both impact parameter and energy dependences. The analogous results are also obtained for  $C_{pp}$  shown in Fig. 5.

The strength of  $C_{pn}$ ,  $C_{nn}$  and  $C_{pp}$  is mainly decided by the distance in phase space at freeze-out time. Under specific entrance channel conditions (high energy and large impact parameter), the size of phase space in final state is consistent with initial size of  $^{15}C$  projectile, which largely depends on the neutron skin structure. This can be seen from Fig. 6 showing impact parameter dependences of RMS radii in coordinate and momentum space. The size of phase space decreases with the increasing of impact parameter. The more extended neutron skin leads to larger RMS radii of coordinate and momentum in final state for peripheral collisions at 800 MeV/nucleon, which results in smaller correlation in the HBT method. However,

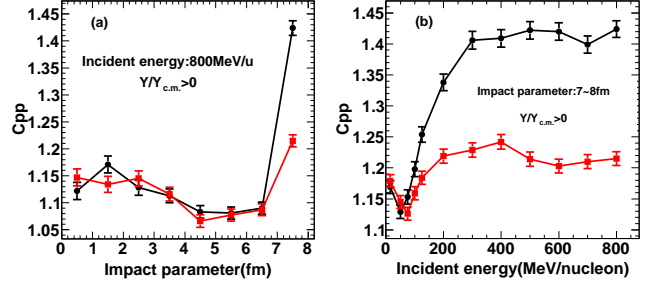


FIG. 5: (Color online) The same as Fig. 3 but for  $C_{pp}$ .

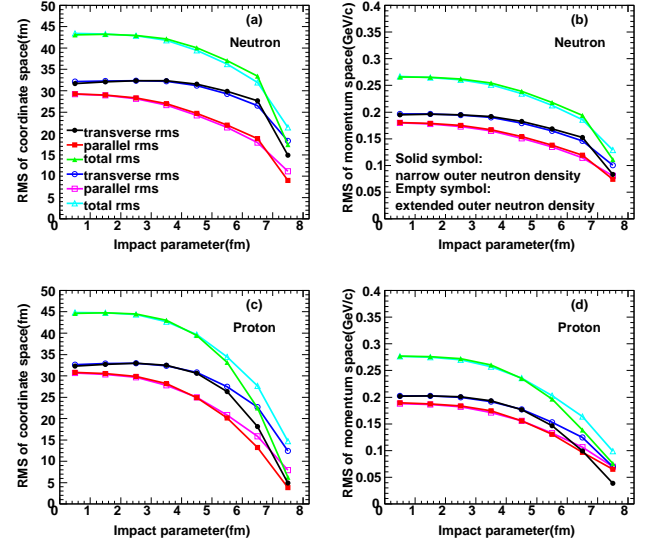


FIG. 6: (Color online) Root-mean-square of coordinate (panel (a) and (c)) and momentum (panel (b) and (d)) space distributions in the center of mass reference frame as a function of impact parameter at incident energy of 800 MeV/nucleon and rapidity  $> 0$  for neutron (panel (a) and (b)) and proton (panel (c) and (d)), respectively. The solid (empty) circles, squares and triangles represent transverse, parallel and total RMS radii, respectively, for  $^{15}C$  projectiles induced collisions, where  $^{15}C$  projectiles are sampled from two density outputs of RMF model with valence neutron on  $1d5/2$  and  $2s1/2$  states, respectively.

RMS radii do not have difference between the two kinds of  $^{15}C$  induced reactions in central and semi-peripheral collisions because the only difference in outer neutron is covered in violent collisions. Therefore, the physical picture of phase space size is consistent with impact parameter dependences of  $C_{pn}$ ,  $C_{nn}$  and  $C_{pp}$ . The excitation function of RMS radii of phase space in peripheral collisions shown in Fig. 7 gradually become saturated at high incident energy, which can explain the saturation of correlations in panel (b) of Fig. 3, 4 and 5.

The space-time extent of emission source for different particles can be extracted from the shape and height of  $C_{pp}$ ,  $C_{nn}$  and  $C_{pn}$  for  $^{15}C$  projectiles with and without neutron skin. Angle-averaged Koonin-Pratt formula can



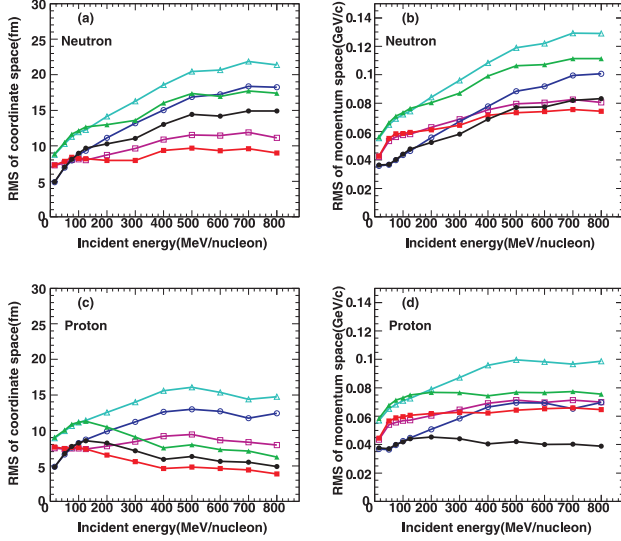


FIG. 7: (Color online) Root-mean-square of coordinate (panel (a) and (c)) and momentum (panel (b) and (d)) space distributions in the center of mass reference frame as a function of incident energy with impact parameter  $b = 7 - 8 fm$  and rapidity  $> 0$  for neutron (panel (a) and (b)) and proton (panel (c) and (d)), respectively. The symbols have the same convention as in Fig. 6.

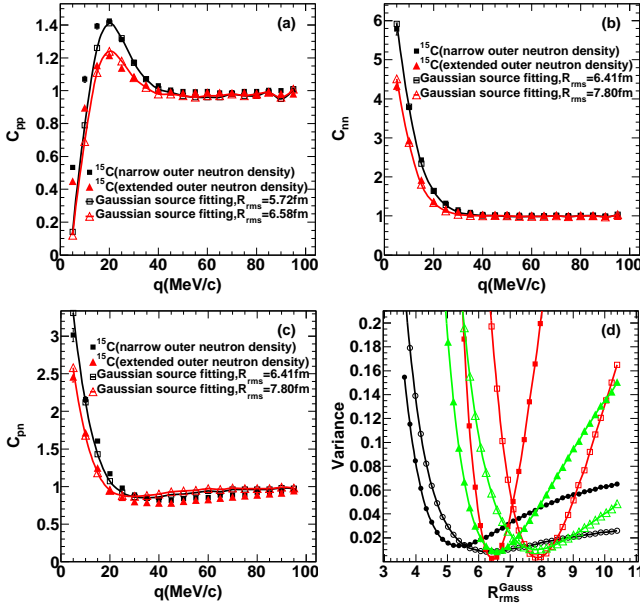


FIG. 8: (Color online) Gaussian source fitting for  $C_{pp}$  (panel (a)),  $C_{nn}$  (panel (b)),  $C_{pn}$  (panel (d)) and variance between IDQMD + CRAB correlation and Gaussian source correlation as a function of Gaussian source size (panel (d)). The entrance channel conditions of 800 MeV/nucleon bombarding energy and impact parameter with  $b = 7 - 8 fm$  are used and the nucleons with rapidity  $> 0$  in final state are chosen.

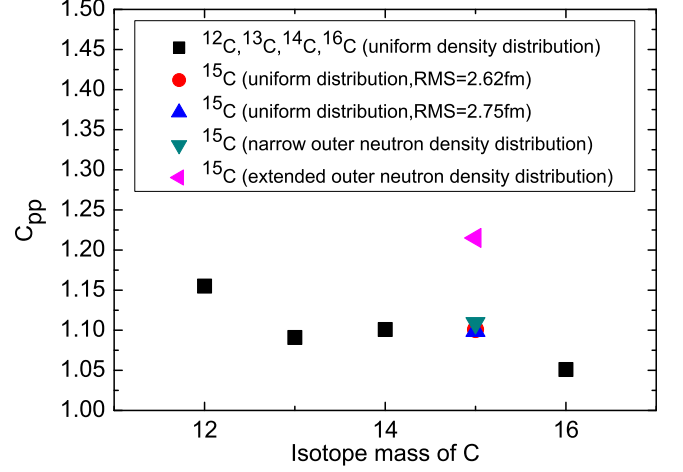


FIG. 9: (Color online) Dependence of  $C_{pp}$  (strength of  $C_{pp}$  at 20 MeV/c) on C isotopes ( $^{12,13,14,15,16}C$ ) induced collisions. Different collision systems are compared with the same reduced impact parameter range: 0.875 – 1.0 and only protons with rapidity  $> 0$  are used to calculate momentum correlation function. Nucleons of  $^{12,13,14,16}C$  are sampled from uniform density. We construct four kinds of  $^{15}C$  projectiles: two of them are sampled from two RMF densities shown in Fig. 1, respectively, and the other two are sampled from uniform distribution with two different sizes, corresponding to the sizes of  $1d5/2$  and  $2s1/2$  states in RMF model, respectively.

be written as [4, 50]:

$$R(q) = 4\pi \int r^2 dr K(q, r) S(r), \quad (5)$$

where  $S(r)$  is the isotropic source function standing for the probability distribution of emitting a pair of nucleons at relative distance  $r$ .  $K(q, r)$  is angle-averaged kernel function obtained from radial part of two-nucleon relative wave function. If we assume  $S(r)$  has simple Gaussian form:

$$S(r) = \frac{1}{(2\pi)^{3/2} \sigma^3} \exp\left(-\frac{r^2}{2\sigma^2}\right), \quad (6)$$

where  $\sigma$  describes the spatial distribution of nucleons emitting location and the RMS radius of Gaussian source equals  $\sqrt{3}\sigma$ . Gaussian source method is used to fit the correlation functions ( $C_{pp}$ ,  $C_{nn}$  and  $C_{pn}$ ) for two kinds of  $^{15}C$  induced collisions. The panel (d) of Fig. 8 represents the variance between IDQMD and Gaussian source correlations as a function of RMS radius of Gaussian source. Then the best fitting is judged by the variance and the RMS radii obtained are shown in panel (a), (b) and (c), respectively. We get the same Gaussian source size from  $C_{nn}$  and  $C_{pn}$ . The emission source size of projectiles with skin structure is about 20% larger than that of projectiles without skin structure for  $C_{nn}$  and  $C_{pn}$ . The source size of  $C_{pp}$  is smaller than that of  $C_{nn}$  and  $C_{pn}$  for both kinds of  $^{15}C$  projectiles. Comparing with initialized neutron distribution shown in Fig. 1 and table I, we can conclude that the initial structure information of

neutron skin and size of projectile is kept till final state. The size of proton emission source is different for the two kinds of  $^{15}\text{C}$  projectiles, though initial density distribution of proton is the same. The size is about 15% larger for projectiles with neutron skin, which proves that proton density distribution is disturbed through interaction with neutron even in very peripheral collisions.

The size of emission source extracted above is under hypothesis that nucleon is expressed by point particle. However, in QMD model, nucleon wave function has Gaussian form in coordinate and momentum space. The true distribution of source is the convolution of the distribution of wave packet center with Gaussian density distribution of single nucleon. In Ref. [51, 52], the relation between RMS radius of the freeze-out points  $\langle r(t)^2 \rangle^{1/2}$  and the variance of the source and wave function is obtained by assuming that a chaotic Gaussian source has formed in collision without correlation between coordinate and momentum space:

$$\langle r(t) \rangle^{1/2} = \sqrt{3(A + L)}, \quad (7)$$

where  $A$  is variance of chaotic emission source with Gaussian form and  $L$  is square of width of Gaussian wave packet in QMD model with value of  $2.16 \text{ fm}^2$  in our calculations. Now with finite width modification of Gaussian wave packet, then we get smaller RMS radius of emission source:  $\sqrt{3A} = \sqrt{3(\sigma^2 - L)}$ . For example, RMS radii of  $C_{pp}$  are  $5.12 \text{ fm}$  and  $6.07 \text{ fm}$  for  $^{15}\text{C}$  projectiles with and without neutron skin, respectively. RMS radii of both  $C_{nn}$  and  $C_{pn}$  have the same value:  $5.88 \text{ fm}$  and  $7.37 \text{ fm}$ , respectively.

We also study the systematical dependence of momentum correlation on other C isotopes induced collisions. Fig. 9 shows the strength of  $C_{pp}$  at 20 MeV/c for  $^{12,13,14,15,16}\text{C} + ^{12}\text{C}$  systems. The collisions are compared at the same reduced parameter range:  $0.875 - 1.0$ . Four kinds of  $^{15}\text{C}$  projectile are constructed. The other two kinds of  $^{15}\text{C}$  projectiles are sampled from uniform density distributions beside the sampling from RMF discussed above. Nucleons are also uniform distribution in  $^{12}\text{C}$ ,  $^{13}\text{C}$ ,  $^{14}\text{C}$  and  $^{16}\text{C}$  projectiles. The total systematical tendency of mass dependence of  $C_{pp}$  is decreasing except for projectiles with neutron skin structure, which can be interpreted as following: though they are simulated at the same reduced impact parameter,  $^{12}\text{C} + ^{12}\text{C}$  collisions have smaller emission source as compared with  $^{16}\text{C} + ^{12}\text{C}$  collisions. Correlation for projectiles with neutron skin is stronger than other cases. This is because that the outer density distribution is more extended due to neutron skin

and then it results in smaller overlap zone between projectile and target for the same reduced impact parameter at peripheral collisions. Therefore, proton-proton has stronger correlation due to they come from one compact projectile-like remnants, which is obvious different from the case without skin structure.

#### IV. SUMMARY

The very small nucleon separation energy of last nucleon and suddenly increased radius compared with its neighboring isotopes are two main features of exotic halo nucleus. HBT method has been used to study the relationship between momentum correlation and single nucleon separation energy several years before. In this paper, we systematically investigate how the density distribution of valence neutron in one-neutron halo candidate  $^{15}\text{C}$  affects the strength of nucleon-nucleon momentum correlation function. Specifically, two kinds of  $^{15}\text{C}$  projectiles are sampled from two different density outputs of RMF model, respectively. The difference of outer neutron density distribution between two kinds of initialized  $^{15}\text{C}$  samples can be viewed as neutron skin structure in IDQMD simulation. The more extended density distribution due to outer neutron in projectile results in the larger and hot emission source, which leads to a larger size of phase space in final state and then corresponds to weaker correlation. The energy and impact parameter dependences show that nucleon-nucleon momentum correlation function is a very sensitive observable of density distribution of valence neutron at high energy and peripheral collisions. Therefore, momentum correlation function at high bombarding energy and large impact parameter can serve as a new potential probe to diagnose the exotic structure such as skin and halo besides the traditional measurements of total reaction cross section and momentum distribution.

#### V. ACKNOWLEDGMENTS

We wish to thank Prof. S. Pratt for providing CRAB code which is used to construct the momentum correlation function from phase space data. This work is partially supported by National Natural Science Foundation of China under contract No.s 11035009, 11005140, 10979074, 10875160, 10805067 and 10975174, and the Knowledge Innovation Project of the Chinese Academy of Sciences under Grant No. KJCX2-EW-N01.

- 
- [1] R. Hanbury Brown and R. Q. Twiss, *Nature* 178 (1956) 1046
  - [2] G. Goldhaber *et al.*, *Phys. Rev.* 120 (1960) 300
  - [3] S. Pratt, M. B. Tsang, *Phys. Rev. C* 36 (1987) 2390
  - [4] S. E. Koonin, *Phys. Lett. B* 70 (1977) 43

- [5] S. Pratt, *Phys. Rev. Lett.* 53 (1984) 1219
- [6] J. P. Sullivan *et al.*, *Phys. Rev. Lett.* 70 (1993) 3000
- [7] D. H. Boal *et al.*, *Rev. Mod. Phys.* 62 (1990) 553
- [8] W. Bauer, C. K. Gelbke and S. Pratt, *Annu. Rev. Nucl. Part. Sci.* 42 (1992) 77

- [9] U. Heinz *et al.*, Annu. Rev. Nucl. Part. Sci. 49 (1999) 529
- [10] U. A. Wiedemann *et al.*, Phys. Rep. 319 (1999) 145
- [11] W. D. Oliver *et al.*, Science 284 (1999) 299
- [12] M. Henny *et al.*, Science 284 (1999) 296
- [13] R. Ghatti, J. Helgesson, V. Avdeichikov *et al.*, Phys. Rev. Lett. 91 (2003) 092701
- [14] G. Verde, A. Chbihi, R. Ghatti *et al.*, Eur. Phys. J. A 30 (2006) 81
- [15] W. G. Gong, W. Bauer, C. K. Gelbke and S. Pratt, Phys. Rev. C 43 (1991) 781
- [16] Y. G. Ma, Y. B. Wei, W. Q. Shen *et al.*, Phys. Rev. C 73 (2006) 014604
- [17] N. Colonna, D. R. Bowman, L. Celano *et al.*, Phys. Rev. Lett. 75 (1995) 4190
- [18] R. Ghatti, V. Avdeichikov, B. Jakobsson *et al.*, Phys. Rev. C 69 (2004) 031605(R)
- [19] L. W. Chen, V. Greco, C. M. Ko and B. A. Li, Phys. Rev. Lett. 90 (2003) 162701
- [20] K. Ieki, D. Sackett, A. Galonsky *et al.*, Phys. Rev. Lett. 70 (1993) 730
- [21] F. M. Marqués, M. Labiche, N. A. Orr *et al.*, Phys. Lett. B 476 (2000) 219
- [22] F. M. Marqués, M. Labiche, N. A. Orr *et al.*, Phys. Rev. C 64 (2001) 061301(R)
- [23] M. T. Yamashita, T. Frederico, L. Tomio, Phys. Rev. C 72 (2005) 011601(R)
- [24] M. Petrascu, A. Constantinescu, I. Cruceru *et al.*, Phys. Rev. C 69 (2004) 011602(R)
- [25] M. Petrascu, A. Constantinescu, I. Cruceru *et al.*, Nucl. Phys. A 790 (2007) 235c
- [26] Y. B. Wei, Y. G. Ma, W. Q. Shen *et al.*, Phys. Lett. B 586 (2004) 225
- [27] Y. B. Wei, Y. G. Ma, W. Q. Shen *et al.*, J. Phys. G 30 (2004) 2019
- [28] Y. G. Ma, X. Z. Cai, J. G. Chen *et al.*, Nucl. Phys. A 790 (2007) 299c
- [29] I. Tanihata, H. Hamagaki, O. Hashimoto *et al.*, Phys. Lett. B 160 (1985) 380
- [30] T. Kobayashi, O. Yamakawa, K. Omata *et al.*, Phys. Rev. Lett. 60 (1988) 2599
- [31] P. Zhou, D. Q. Fang, Y. G. Ma *et al.*, Int. J. Mod. Phys. E 19 (2010) 957
- [32] X. Y. Sun, J. G. Chen, D. Q. Fang *et al.*, Int. J. Mod. Phys. E 19 (2010) 1823
- [33] G. Audi, A. H. Wapstra, C. Thibault, Nucl. Phys. A 729 (2003) 337
- [34] D. Bazin, W. Benenson, B. A. Brown *et al.*, Phys. Rev. C 57 (1998) 2156
- [35] D. Q. Fang, T. Yamaguchi, T. Zheng *et al.*, Phys. Rev. C 69 (2004) 034613
- [36] G. Murillo, S. Sen, and S. E. Darben, Nucl. Phys. A 579 (1994) 125
- [37] A. Ozawa, T. Suzuki and I. Tanihata, Nucl. Phys. A 693 (2001) 32
- [38] D. Q. Fang, W. Q. Shen, J. Feng *et al.*, Phys. Rev. C 61 (2000) 064311
- [39] A. Ozawa, I. Tanihata, T. Kobayashi *et al.*, Nucl. Phys. A 608 (1996) 63
- [40] S. Pratt, J. Sullivan, H. Sorge *et al.*, Nucl. Phys. A 566 (1994) 103c
- [41] J. Aichelin, A. Rosenhauer, G. Peilert, H. Stoecker and W. Greiner, Phys. Rev. Lett. 58 (1987) 1926
- [42] J. Aichelin, Phys. Rep. 202 (1991) 233
- [43] G. Peilert, H. Stöcker, W. Greiner *et al.*, Phys. Rev. C 39 (1989) 1402
- [44] T. Z. Yan, Y. G. Ma, X. Z. Cai *et al.*, Phys. Lett. B 638 (2006) 50
- [45] X. G. Cao, G. Q. Zhang, X. Z. Cai *et al.*, Phys. Rev. C 81 (2010) 061603(R)
- [46] G. Q. Zhang, Y. G. Ma, X. G. Cao and C. L. Zhou, Phys. Rev. C 83 (2011) 064607
- [47] G. Q. Zhang, Y. G. Ma, X. G. Cao, C. L. Zhou, X. Z. Cai, D. Q. Fang, W. D. Tian and H. W. Wang, Phys. Rev. C 84 (2011) 034612
- [48] I. Angeli, At. Data Nucl. Data Tables 87 (2004) 185
- [49] L. W. Chen, V. Greco, C. M. Ko and B. A. Li, Phys. Rev. C 68 (2003) 014605
- [50] G. Verde, D. A. Brown, P. Danielewicz *et al.*, Phys. Rev. C 65 (2002) 054609
- [51] J. Aichelin, Nucl. Phys. A 617 (1997) 510
- [52] F. Gastineau and J. Aichelin, Phys. Rev. C 65 (2001) 014901